

## MATERIALS SCIENCE

# Single-atom doping of MoS<sub>2</sub> with manganese enables ultrasensitive detection of dopamine: Experimental and computational approach

Yu Lei<sup>1,2,3,4,\*</sup>, Derrick Butler<sup>3,4,5\*</sup>, Michael C. Lucking<sup>6</sup>, Fu Zhang<sup>2,3,4,7</sup>, Tunan Xia<sup>8</sup>, Kazunori Fujisawa<sup>1,2,3</sup>, Tomotaroh Granzier-Nakajima<sup>1,2</sup>, Rodolfo Cruz-Silva<sup>9</sup>, Morinobu Endo<sup>9</sup>, Humberto Terrones<sup>6</sup>, Mauricio Terrones<sup>1,2,3,4,7,9,10†</sup>, Aida Ebrahimi<sup>2,3,4,5,7,11†</sup>

Two-dimensional transition metal dichalcogenides (TMDs) emerged as a promising platform to construct sensitive biosensors. We report an ultrasensitive electrochemical dopamine sensor based on manganese-doped MoS<sub>2</sub> synthesized via a scalable two-step approach (with Mn ~2.15 atomic %). Selective dopamine detection is achieved with a detection limit of 50 pM in buffer solution, 5 nM in 10% serum, and 50 nM in artificial sweat. Density functional theory calculations and scanning transmission electron microscopy show that two types of Mn defects are dominant: Mn on top of a Mo atom (Mn<sub>topMo</sub>) and Mn substituting a Mo atom (Mn<sub>Mo</sub>). At low dopamine concentrations, physisorption on Mn<sub>Mo</sub> dominates. At higher concentrations, dopamine chemisorbs on Mn<sub>topMo</sub>, which is consistent with calculations of the dopamine binding energy (2.91 eV for Mn<sub>topMo</sub> versus 0.65 eV for Mn<sub>Mo</sub>). Our results demonstrate that metal-doped layered materials, such as TMDs, constitute an emergent platform to construct ultrasensitive and tunable biosensors.

## INTRODUCTION

Dopamine (DA) is an important neurotransmitter and plays a critical role in a number of physiological processes, including neural signaling, vasodilation outside the brain, and reward processes in the brain (1). Abnormal levels of DA can be indicative of, or lead to, a number of disorders, such as Parkinson's disease, Alzheimer's disease, schizophrenia, or pheochromocytoma (2). In schizophrenic patients, Bird *et al.* (3) discovered elevated DA levels (by 30 to 50%) in certain regions of the brain (specifically, the nucleus accumbens and anterior perforated substance). On the other hand, patients with Parkinson's disease and dementia with Lewy bodies show reduced levels of DA in their brains (2).

Detection of DA can be carried out using a variety of methods, such as mass spectrometry (4), liquid chromatography (4), and electrochemical detection (5). Clinical DA tests for pheochromocytoma and other catecholamine-secreting tumors involve collection and storage of a patient's urine, followed by testing (6). In recent years, research has concentrated on the development of low-cost diagnostics to provide a prompt readout to the user at the point of need. Non-

invasive electrochemical biosensors have become a benchmark in the biosensor community because of their high sensitivity, relatively low cost, short response time, and compatibility with integrated circuit technology for easy readout. Furthermore, because DA is a highly redox-active molecule, electrochemical detection is an innate choice for its detection. Previous reports of low concentration (pM) detection of DA do exist (7). Although these reports demonstrate remarkable DA detection capabilities, they use precious metals or biological capture molecules, such as nucleic acids, aptamers, or enzymes, that add to the fabrication complexity, thereby increasing overall cost and limiting the scalability.

Two-dimensional (2D) materials have emerged as a rising material platform to construct flexible and ultrasensitive sensors, including DA sensors (5). 2D materials share the advantages of high surface-to-volume ratio, the ability to scale down to a monolayer, robust covalent bonding within the layer, and tunable electronic/optical properties (8, 9). Specifically, graphene (the "mother" of all 2D materials) stands out as an efficient DA sensor because of its biocompatibility, high electrical conductivity, and strong  $\pi$ - $\pi$  interactions with DA (10). However, pristine graphene is a zero-bandgap material with a lack of dangling bonds on its surface (11). Therefore, defects are typically necessary to open up the bandgap of graphene so that an efficient band alignment with a target analyte can be achieved (10). Instead, owing to their finite and tunable bandgap, transition metal dichalcogenides (TMDs) have a broad range of electronic properties, from insulators, semiconductors, and semimetals to true metals (12). Among them, MoS<sub>2</sub>, a semiconducting TMD with an indirect bandgap of 1.29 eV in the bulk and a direct bandgap of ~1.9 eV in the monolayer form (13), has been demonstrated as an effective material for DA detection (5). However, additional surface functionalization is still needed to facilitate the adsorption of the biomolecule to the surface. Hence, noble metal particles, such as gold (Au) (5, 14), are commonly used to form composites with MoS<sub>2</sub> for the selective detection of DA. Considering the scarcity and cost of noble metals, it is necessary to find a lower cost alternative. In

Copyright © 2020  
The Authors, some  
rights reserved;  
exclusive licensee  
American Association  
for the Advancement  
of Science. No claim to  
original U.S. Government  
Works. Distributed  
under a Creative  
Commons Attribution  
NonCommercial  
License 4.0 (CC BY-NC).

<sup>1</sup>Department of Physics, The Pennsylvania State University, University Park, PA 16802, USA. <sup>2</sup>Center for Two-Dimensional and Layered Materials, The Pennsylvania State University, University Park, PA 16802, USA. <sup>3</sup>Center for Atomically Thin Multifunctional Coatings, The Pennsylvania State University, University Park, PA 16802, USA. <sup>4</sup>Materials Research Institute, The Pennsylvania State University, University Park, PA 16802, USA. <sup>5</sup>School of Electrical Engineering and Computer Science, The Pennsylvania State University, University Park, PA 16802, USA. <sup>6</sup>Department of Physics, Applied Physics, and Astronomy, Rensselaer Polytechnic Institute, Troy, NY 12180, USA. <sup>7</sup>Department of Materials Science and Engineering, The Pennsylvania State University, University Park, PA 16802, USA. <sup>8</sup>National Laboratory of Solid-State Microstructures and School of Physics, Nanjing University, Nanjing 210093, People's Republic of China. <sup>9</sup>Initiative for Supra-Materials and Global Aqua Innovation Center, Shinshu University, 4-17-1-1 Wakasato, Nagano 380-8553, Japan. <sup>10</sup>Department of Chemistry, The Pennsylvania State University, University Park, PA 16802, USA. <sup>11</sup>Department of Biomedical Engineering, The Pennsylvania State University, University Park, PA 16802, USA.

\*These authors contributed equally to this work.

†Corresponding author. Email: sue66@psu.edu (A.E.); mut11@psu.edu (M.T.)

this context, doping with heteroatoms provides a unique opportunity to modify and functionalize the surface of layered materials (15). Doping not only introduces localized gap states that modulate electronic properties but also can improve the adsorption of molecules (15). Moreover, selectivity can be achieved by heteroatom doping. For example, manganese (Mn) has been considered as an efficient catalytic site to oxidize DA through redox cycling between Mn(II)/Mn(III) (16, 17). Thus, we hypothesized that incorporating Mn in MoS<sub>2</sub> could significantly improve the selectivity of DA detection.

In this work, we design and fabricate Mn-MoS<sub>2</sub> electrodes for the electrochemical identification of DA down to a concentration of 50 pM in phosphate-buffered saline (PBS) exhibiting two dynamic ranges of 50 pM to 5 nM and 5 nM to 5  $\mu$ M. A scalable synthesis method is developed for the electrodeposition of MoS<sub>2</sub> on pyrolytic graphite sheets (PGSs), followed by thermal doping of MoS<sub>2</sub> with Mn. Using scanning transmission electron microscopy (STEM) and X-ray photoelectron spectroscopy (XPS), it is observed that ~68% of Mn atoms substitutionally dope MoS<sub>2</sub>, whereas ~32% of Mn atoms are adatoms. The incorporation of Mn dopants leads to improved electrochemical behavior toward DA compared to bare PGS and undoped MoS<sub>2</sub>. Specifically, Mn-MoS<sub>2</sub> exhibits outstanding performance in the selective detection of DA versus other common redox-active interferents, including ascorbic acid (AA) and uric acid (UA). Moreover, Mn-MoS<sub>2</sub> shows a DA detection limit of 5 nM in serum and 50 nM in artificial sweat. Density functional theory (DFT) calculations are carried out on several possible Mn defect locations within the MoS<sub>2</sub> lattice. We calculate that Mn substituting Mo atoms (Mn<sub>Mo</sub>) is energetically favorable and induces a better alignment between the highest occupied molecular orbital of DA and the valence band of Mn-MoS<sub>2</sub> compared to other defect configurations, such as Mn adatoms on top of Mo (Mn<sub>topMo</sub>). Our calculations demonstrate that Mn<sub>Mo</sub> defects lead to the physisorption of DA molecules rather than chemisorption (as in the case of the Mn<sub>topMo</sub> defect).

## RESULTS

### Material synthesis and characterization

Mn-doped MoS<sub>2</sub> is synthesized via a two-step approach involving step 1 (electrodeposition) and step 2 (solid-vapor deposition) (Fig. 1A). Amorphous MoS<sub>2</sub> is first electrodeposited on a PGS (MTI Corp.) to create MoS<sub>2</sub>/PGS. Because of the lack of crystalline bonds in the deposited amorphous MoS<sub>2</sub>, heteroatoms are able to be incorporated into MoS<sub>2</sub>. Here, a solid-vapor deposition is used to introduce Mn atoms, while the amorphous MoS<sub>2</sub> becomes crystallized. The Raman spectrum of 2H MoS<sub>2</sub> (fig. S1) shows the in-plane ( $E_{2g}^1$ ) and out-of-plane vibration ( $A_{1g}$ ) modes around 384.0 and 411.4 cm<sup>-1</sup>, respectively. After Mn doping, the  $E_{2g}^1$  remains unchanged, but the  $A_{1g}$  mode shifts from 411.4 cm<sup>-1</sup> in MoS<sub>2</sub> to 408.6 cm<sup>-1</sup> in Mn-MoS<sub>2</sub>/PGS, which is due to a strong electron-phonon coupling of the  $A_{1g}$  mode after doping [e.g., Nb doping; (18)].

The energy-dispersive X-ray spectroscopy (EDS) mappings (Fig. 1B) indicate that the distribution of Mn is correlated with Mo and S with mild oxidation. STEM coupled with high-angle annular dark-field (HAADF) imaging with atomic resolution reveals the fine structure of the Mn-MoS<sub>2</sub> based on the Z-contrast difference between Mn ( $Z_{Mn} = 25$ ) and Mo ( $Z_{Mo} = 42$ ), where Z is the atomic number (19). As seen in fig. S2A, Mn<sub>Mo</sub> and Mn<sub>topMo</sub> can be both found in Mn-MoS<sub>2</sub>, and the distribution reveals that ~68% of Mn

atoms are Mn<sub>Mo</sub>. Because of the Z-contrast mechanism, Mn atoms show a weaker contrast when compared to Mo if they are substitutionally doping MoS<sub>2</sub> (Fig. 1C). On the contrary, if Mn atoms are bonded as adatoms on top of the Mo atoms, they have brighter contrast than Mo as seen in Fig. 1D. In addition, the HAADF-STEM image intensity line profiles also reveal that Mn atoms are doped as both Mn<sub>Mo</sub> and Mn<sub>topMo</sub>; Mn atoms are all bonded to S atoms, thus matching the simulated image line profiles (Fig. 1, C and D). This is also confirmed by the presence of Mn-S bonds in the XPS spectra (fig. S3). On the basis of the Mn 2p core level (fig. S3A), the peaks located at 642.0 and 653.5 eV can be assigned to Mn 2p<sub>3/2</sub> and Mn 2p<sub>1/2</sub> for Mn-S bonds (20). Because of oxidation, Mn-O bonds can also be found with a spin-orbit splitting of 11.8 eV (21). According to the S 2p core level (fig. S3B), the Mn-S bonds located at 162.0 eV (S 2p<sub>3/2</sub>) can be clearly observed, together with Mo-S bonds at 162.3 eV (S 2p<sub>3/2</sub>) in Mn-MoS<sub>2</sub> (20). On the basis of the XPS results, the total incorporation of Mn in Mn-MoS<sub>2</sub> is ~2.15 atomic % as indicated in table S1. By comparing the x-ray diffraction (XRD) patterns of the Mn-MoS<sub>2</sub>, MoS<sub>2</sub>, and the PGS substrate (fig. S4), only the additional (002) peaks of MoS<sub>2</sub> can be found in Mn-MoS<sub>2</sub>, indicating that Mn atoms are mainly doping the MoS<sub>2</sub> sheets rather than forming into crystalline Mn clusters.

### Electrochemical characterization

To understand and compare the charge transfer characteristics of PGS, MoS<sub>2</sub>/PGS, and Mn-MoS<sub>2</sub>/PGS samples, we use electrochemical impedance spectroscopy (EIS) and cyclic voltammetry (CV). A schematic of the electrochemical testing setup is shown in Fig. 2A. To better understand the modulation of electroactivity, surface functionalities, and the effective surface area after each synthesis step, we use three redox-active compounds, namely, [Fe(CN)<sub>6</sub>]<sup>3-/4-</sup>, an inner-sphere redox probe, [Ru(NH<sub>3</sub>)<sub>6</sub>]<sup>2+/3+</sup>, an outer-sphere redox probe (both 5 mM in PBS), and 50  $\mu$ M DA in PBS. While outer-sphere probes do not chemically interact with the electrode surface, inner-sphere probes are affected more by surface chemistry and the electron transfer between electrode and probe molecule can vary drastically in the presence of various surface functionalities (22). Hence, both types of redox probes are used to compare PGS, MoS<sub>2</sub>/PGS, and Mn-MoS<sub>2</sub>/PGS samples.

Figure S5 shows the CV curves for [Ru(NH<sub>3</sub>)<sub>6</sub>]<sup>2+/3+</sup> and [Fe(CN)<sub>6</sub>]<sup>3-/4-</sup> redox probes. For [Ru(NH<sub>3</sub>)<sub>6</sub>]<sup>2+/3+</sup>, a decrease in the Faradaic peak separation ( $\Delta E_p$ ) of 30 mV is observed in Mn-MoS<sub>2</sub>/PGS when compared to PGS and MoS<sub>2</sub>/PGS ( $\Delta E_p = 110$  mV for both), corresponding to a 27% decrease. Such a decrease in the peak separation indicates an improvement in the reaction kinetics (23). The Faradaic peak current ratio (i.e., the ratio of oxidation to reduction peak currents,  $I_{o/r} \equiv I_{ox}/I_{red}$ ) also shifts closer to unity for Mn-MoS<sub>2</sub>/PGS ( $I_{o/r} = 0.91$ ) compared to 0.79 and 0.84 for PGS and MoS<sub>2</sub>/PGS, respectively. Similar to  $\Delta E_p$ , the peak current ratio benchmarks the electrochemical performance of a material, with a value of 1 corresponding to ideal electrochemical reversibility (23). The absolute current values are very similar in all three samples, implying that the effective surface area is roughly the same. Figure S5B shows the CV data of each electrode using the [Fe(CN)<sub>6</sub>]<sup>3-/4-</sup> inner-sphere redox probe. A drastic improvement in  $\Delta E_p$  can be seen for both Mn-MoS<sub>2</sub>/PGS ( $\Delta E_p = 700$  mV) and MoS<sub>2</sub>/PGS ( $\Delta E_p = 570$  mV) when compared to PGS ( $\Delta E_p = 930$  mV). The peak current ratio also shifts closer to unity for Mn-MoS<sub>2</sub>/PGS ( $I_{o/r} = 2.67$ ) as opposed to PGS ( $I_{o/r} = 3.42$ ) and MoS<sub>2</sub>/PGS ( $I_{o/r} = 3.77$ ), which corresponds

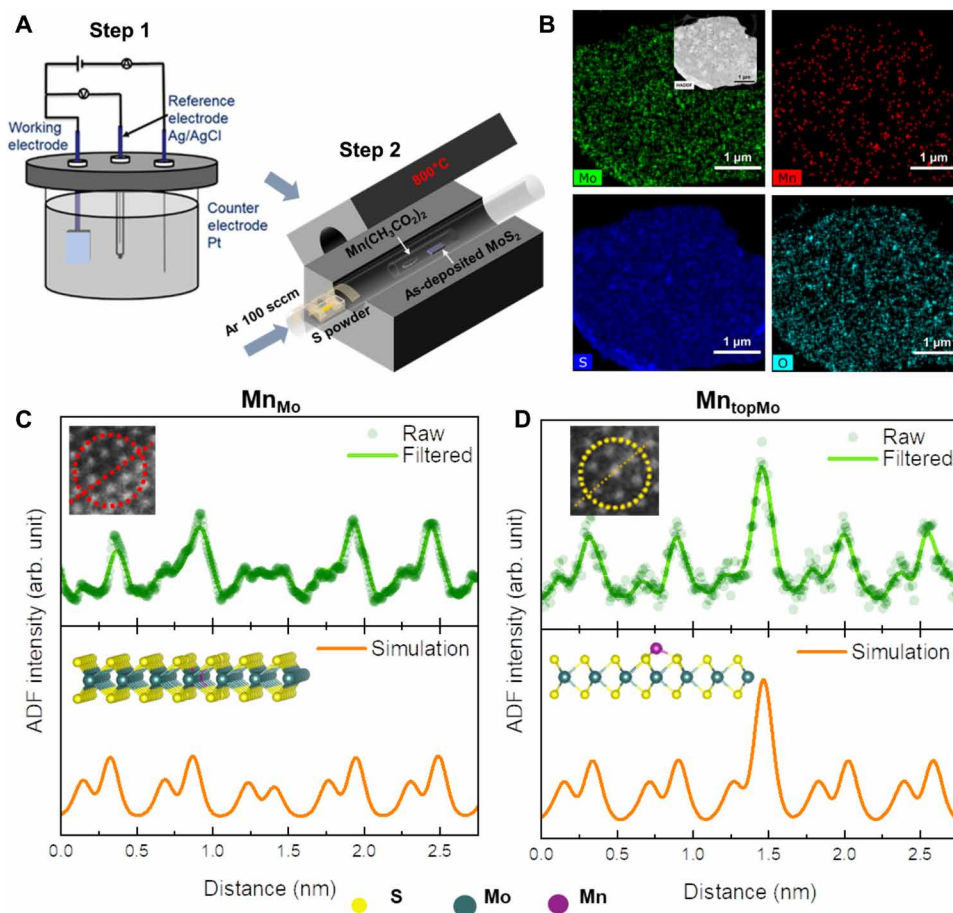


**Fig. 1. Materials synthesis and confirmation of the presence of Mn atoms.** (A) Schematic of the two-step synthesis of Mn-MoS<sub>2</sub>: Step 1: MoS<sub>2</sub> electrodeposition on PGS in a three-electrode electrochemical cell. Step 2: Mn doping via solid-vapor deposition. (B) EDS mappings (Mo, Mn, S, and O) of Mn-MoS<sub>2</sub>, and the inset is the STEM image of the mapping area. Experimental and simulated HAADF intensity profiles corresponding to (C) Mn<sub>Mo</sub> and (D) Mn<sub>topMo</sub>. The STEM images and the structures are shown in the insets.

to ca. 30% improvement. Characterization with [Ru(NH<sub>3</sub>)<sub>6</sub>]<sup>2+/3+</sup> and [Fe(CN)<sub>6</sub>]<sup>3-/4-</sup> shows a shift toward more ideal values (i.e.,  $I_{o/r} = 1$  and  $\Delta E_p = \frac{59.2}{n}$  mV at room temperature, where  $n$  = number of electrons transferred in reaction) for Mn-MoS<sub>2</sub>/PGS compared to PGS and MoS<sub>2</sub>/PGS, with the exception of  $\Delta E_p$  for Mn-MoS<sub>2</sub>/PGS being greater than  $\Delta E_p$  for MoS<sub>2</sub>/PGS with [Fe(CN)<sub>6</sub>]<sup>3-/4-</sup>. A possible cause for a larger  $\Delta E_p$  (i.e., slower charge transfer) for Mn-MoS<sub>2</sub>/PGS as opposed to MoS<sub>2</sub>/PGS may be due to an increase in the negative charge at the Mn-MoS<sub>2</sub>/PGS electrode, thereby repelling the negatively charged [Fe(CN)<sub>6</sub>]<sup>3-/4-</sup> more readily (24).

EIS provides a means to better understand the electrode/solution interface and the electrochemical reactions with a target analyte (here, DA) (25). Using 50 μM DA as a redox probe, EIS measurements are performed on PGS, MoS<sub>2</sub>/PGS, and Mn-MoS<sub>2</sub>/PGS electrodes. Here, a DC potential ( $E_{dc}$ ) of 0.1 V versus open-circuit potential (OCP) and an AC potential of 10 mV are applied to the electrodes. The Nyquist data are fit with a Randles equivalent circuit (Fig. 2B) composed of a solution resistance ( $R_{sol}$ ), charge transfer resistance ( $R_{ct}$ ), double-layer constant phase element (CPE;  $Q_{dl}$ ), and a Warburg impedance element ( $Z_W$ ). A CPE is used instead of a standard capacitor to account for non-idealities in the system (e.g., surface roughness). Typical fitted values of the exponent ( $n$ ) in the CPE

impedance ( $Z = \frac{1}{Q(i\omega)^n}$ ) are ~0.9, with a value of 1 representing an ideal capacitor. Figure 2B shows the EIS data for each electrode, swept over a range of frequencies from 100 mHz to 1 MHz. The  $R_{ct}$  of the PGS sample is  $\sim(9.11 \pm 0.8) \times 10^5$  ohms, with less than 10% fitting error. The inset of Fig. 2B provides a closer look at the high-frequency regions of the MoS<sub>2</sub>/PGS and Mn-MoS<sub>2</sub>/PGS spectra. The  $R_{ct}$  of MoS<sub>2</sub>/PGS is  $(7.10 \pm 0.4) \times 10^4$  ohms, which is larger than that of Mn-MoS<sub>2</sub>/PGS [ $(4.49 \pm 0.5) \times 10^4$  ohms]. The decrease in charge transfer resistance toward DA upon the addition of Mn to the MoS<sub>2</sub>/PGS electrode suggests more favorable kinetics compared to MoS<sub>2</sub>/PGS and PGS.

### Sensing performance

Among various electrochemical sensing methods, differential pulse voltammetry (DPV) is one of the most commonly used techniques, in which square pulses are imposed upon a linear potential sweep. High sensitivity with DPV is achieved because of “filtering” of the non-Faradaic current by sampling the current before and at the end of each pulse. Figure 2C shows DPV data obtained using Mn-MoS<sub>2</sub>/PGS with concentrations ( $\rho_{DA}$ ) ranging from 50 pM to 50 μM in PBS solution (pH 7.2). The DA oxidation peak currents increase with concentration, with a limit of detection (LoD) of ~50 pM for



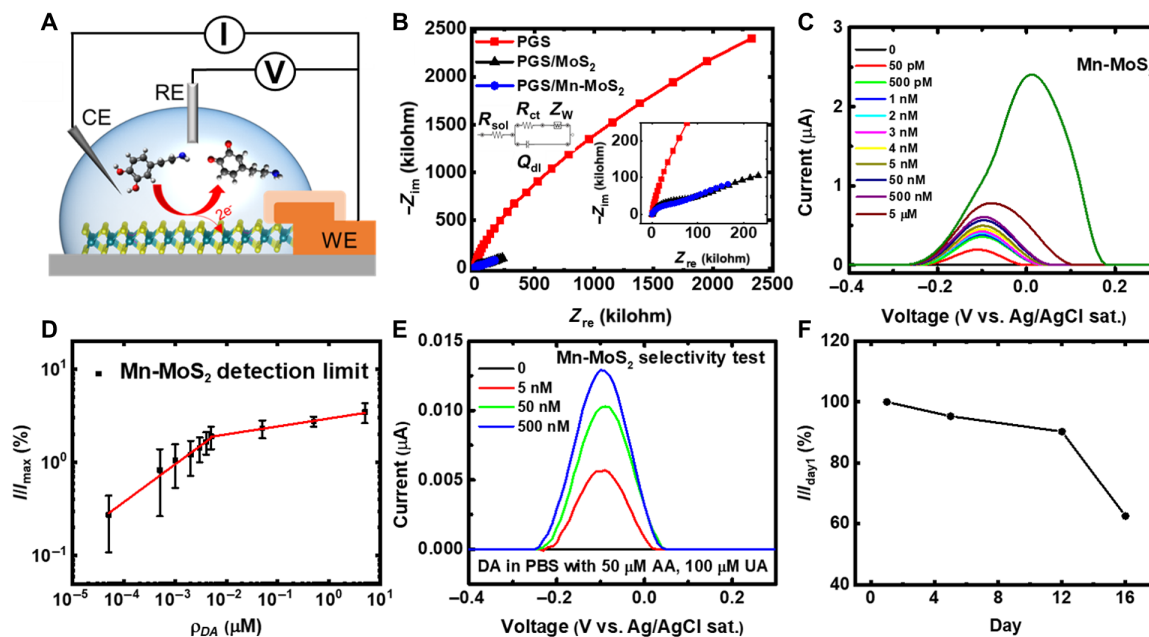


**Fig. 2. Electrochemical characterization and sensing performance of Mn-MoS<sub>2</sub> and MoS<sub>2</sub> on PGS.** (A) Schematic of the electrochemical testing setup. (B) The EIS results for each electrode in 50  $\mu\text{M}$  DA in PBS. The Mn-MoS<sub>2</sub>/PGS shows the lowest charge transfer resistance ( $4.49 \times 10^4$  ohms) followed by MoS<sub>2</sub>/PGS ( $7.10 \times 10^4$  ohms) and PGS ( $9.11 \times 10^5$  ohms). The inset shows a closer view of the MoS<sub>2</sub> and Mn-MoS<sub>2</sub> spectra. (C) DPV data of different  $\rho_{\text{DA}}$  in PBS using Mn-MoS<sub>2</sub>/PGS. (D) Calibration curves  $I_{\text{Imax}} (\%)$  versus  $\rho_{\text{DA}}$  derived from the DPV data shown in (C). (E) DPV results for different  $\rho_{\text{DA}}$  in PBS containing 50  $\mu\text{M}$  AA and 100  $\mu\text{M}$  UA using Mn-MoS<sub>2</sub>/PGS. (F) Lifetime measurements using Mn-MoS<sub>2</sub>/PGS:  $I_{\text{Iday1}} (\%)$  versus day.

Mn-MoS<sub>2</sub>/PGS, while the LoD of undoped MoS<sub>2</sub>/PGS is four orders of magnitude higher (ca. 500 nM), as seen in fig. S6. The substantial improvement of the detection limit is consistent with the improved charge transfer resistance of Mn-MoS<sub>2</sub>/PGS when compared to the other two samples (i.e.,  $R_{\text{ct}}^{\text{Mn-MoS}_2} < R_{\text{ct}}^{\text{MoS}_2} < R_{\text{ct}}^{\text{PGS}}$ ). On the basis of the calibration curve (Fig. 2D), the signal (Eq. 1) is proportional to the  $\log(\rho_{\text{DA}})$  in the range of 50 pM to 5 nM. The corresponding regression equation is provided in Eq. 2 with a correlation coefficient of 0.9928. As the DA concentration increases, the surface of Mn-MoS<sub>2</sub> is saturated with DA, and the increase in the peak current becomes slower, thus resulting in another regression equation (Eq. 3) with a correlation coefficient of 0.9967

$$\log(I_n) \triangleq \log\left(\frac{I}{I_{\text{max}}} \times 100 \%\right) \quad (1)$$

$$\log I_n = 1.194 + 0.405 \log \rho_{\text{DA}} \quad (2)$$

$$\log I_n = 0.470 + 0.085 \log \rho_{\text{DA}} \quad (3)$$

From the DPV data shown in Fig. 2C, we observe that as  $\rho_{\text{DA}}$  increases from 50 nM to 5  $\mu\text{M}$ , the DPV peak shifts to more positive values. When  $\rho_{\text{DA}}$  further increases to 5 mM (fig. S7A), the shift is almost 300 mV (fig. S7B). These shifts are generally attributed to a decreased diffusion coefficient and hence slower electron transfer when  $\rho_{\text{DA}}$  increases; thus, a more positive potential is needed to overcome the kinetic barrier (26). However, by comparing the calibration curves shown in Fig. 2D and the peak shift plot in fig. S7B, the potential shift is negligible ( $\sim 10$  mV) from 50 pM to 5 nM, corresponding to the first linear region (Eq. 2), but a more obvious

shift ( $\sim 300$  mV) is obtained from 5 nM to 5 mM, which corresponds to the second linear region (Eq. 3). At higher concentrations, the peak shifts can also be attributed to surface fouling from by-products of DA oxidation (27). Other than that, as discussed in the DFT section, the contribution of Mn<sub>topMo</sub> defects, which involves chemisorption of DA on the sensor, increases with DA concentration. The enhanced chemisorption may also explain the noticeable shift of the peak potential from 50 nM to 5 mM. At concentrations below 50 nM (more physiologically relevant), the contribution of Mn<sub>Mo</sub> defects (interacting with DA through physisorption) is more dominant, thereby explaining the noteworthy improvement of sensing performance at low DA concentrations. Therefore, two distinct dynamic regions are obtained in the calibration curves shown in Fig. 2D.

Besides sensitivity, selectivity is another essential figure of merit for any sensor. In the extracellular fluids of the central nervous system and serum in mammals, AA and UA always coexist with DA (14). Thus, it is essential to selectively detect DA in the presence of these redox-active interferents. To evaluate the selectivity of Mn-MoS<sub>2</sub>/PGS sensors toward DA, we test solutions of AA and UA in PBS (see fig. S8). No oxidation peak for AA is seen in the concentration range tested, while a peak can be seen for UA around  $-0.1$  V similar to that of DA, although the peak magnitudes are much less than for DA. The peak currents at different concentrations of each analyte are compared in fig. S8D, demonstrating that Mn-MoS<sub>2</sub>/PGS is substantially more responsive to DA than UA and AA. This improved response indicates favorable adsorption of DA on the surface of Mn-MoS<sub>2</sub>/PGS over AA and UA at the same condition. Furthermore, amperometric tests are conducted to evaluate the real-time response of the Mn-MoS<sub>2</sub> sensor to DA, as well as several other common physiological interferents (fig. S8E). The Mn-MoS<sub>2</sub> sensor is highly selective toward DA oxidation while demonstrating

little to no response to other common physiological interferents at the applied potential of 0.15 V. Continuing with this theme, Mn-MoS<sub>2</sub> is then tested in a mixed solution with increasing  $\rho_{\text{DA}}$ , while  $\rho_{\text{AA}}$  and  $\rho_{\text{UA}}$  are kept at 100 and 50  $\mu\text{M}$ , respectively. As seen in Fig. 2E, the peak current increases, with  $\rho_{\text{DA}}$  ranging from 5 nM to 50  $\mu\text{M}$ , and the presence of UA and AA has an insignificant effect on the sensor performance. The DA selectivity is due to the catalytic behavior of the Mn dopants, where the redox couple Mn(II)/Mn(III) is considered as the catalytic sites for DA oxidation (16, 17). Besides sensitivity and selectivity, the Mn-MoS<sub>2</sub>/PGS sensor is environmentally stable in air. The response of the Mn-MoS<sub>2</sub>/PGS sensor toward 5  $\mu\text{M}$  DA is recorded every ~5 days (Fig. 2F). After 12 days, there is only a 10% degradation in the peak current, revealing good ambient stability.

To demonstrate the application of Mn-MoS<sub>2</sub>/PGS for quantification of an analyte in physiological conditions, which is important for point-of-care diagnostics, we explore the sensing performance of Mn-MoS<sub>2</sub>/PGS for detection of DA in artificial sweat. Our results, as shown in Fig. 3A, indicate that the Mn-MoS<sub>2</sub>/PGS sensor is able to detect DA concentrations as low as 50 nM in artificial sweat containing 5 mM glucose. To the best of our knowledge, there are no reports on sensing DA in sweat despite the fact that many of the biomarkers found in blood are also found in sweat, albeit at lower concentrations (28). In addition, the Mn-MoS<sub>2</sub>/PGS sensor is able to detect DA in another biologically complex sample, namely, serum, with a detection limit at 5 nM. Our results provide the first step in demonstrating Mn-MoS<sub>2</sub> as a low-cost sensitive material for non-invasive monitoring of DA levels in sweat using wearable technologies.

In addition, as a proof of concept and to demonstrate the compatibility of Mn-MoS<sub>2</sub> for integration with flexible platforms, we fabricate an all-integrated sensor on a flexible polyimide (PI) substrate. Traditional electrochemical setups, with bulky reference electrodes (REs), can be cumbersome and pose a challenge in the pursuit of miniaturization and portability. Hence, these setups are not conducive to point-of-care monitoring. Here, Mn-MoS<sub>2</sub>/PGS is used as the working electrode (WE), PGS as the counter electrode (CE), and silver (Ag) paste as the pseudo-RE. A schematic of the sensor is shown in Fig. 3C with the resulting sensor response to DA in PBS, thereby transitioning from traditional electrochemical testing schemes toward potential point-of-care applications. After baseline subtraction, the sensor is able to successfully detect as low as 500 nM.

Overall, the Mn-MoS<sub>2</sub>/PGS sensor shows an ultralow LoD for DA (50 pM in PBS, 5 nM in 10% serum, and 50 nM in sweat). The sensor enables a wide dynamic range for detection of DA from 50 pM to 5  $\mu\text{M}$  (defined by two fitting equations, Eqs. 2 and 3). Table 1 provides a comparison of Mn-MoS<sub>2</sub>/PGS with a selection of contemporary electrochemical DA sensing methods reported in the literature. This work demonstrates an improved LoD compared to other works. The selectivity is comparable to the existing reports. However, compared to most other studies (focusing on PBS as the electrolyte), Mn-MoS<sub>2</sub>/PGS is an effective material for DA detection in sweat, offering alternative opportunities for developing noninvasive diagnostics.

### DFT calculations

To better understand the improved charge transfer and significantly higher sensitivity of Mn-MoS<sub>2</sub>/PGS compared to pristine MoS<sub>2</sub>/PGS samples, the electronic structure and energetics of several Mn defects in the MoS<sub>2</sub> lattice have been computed using DFT. The

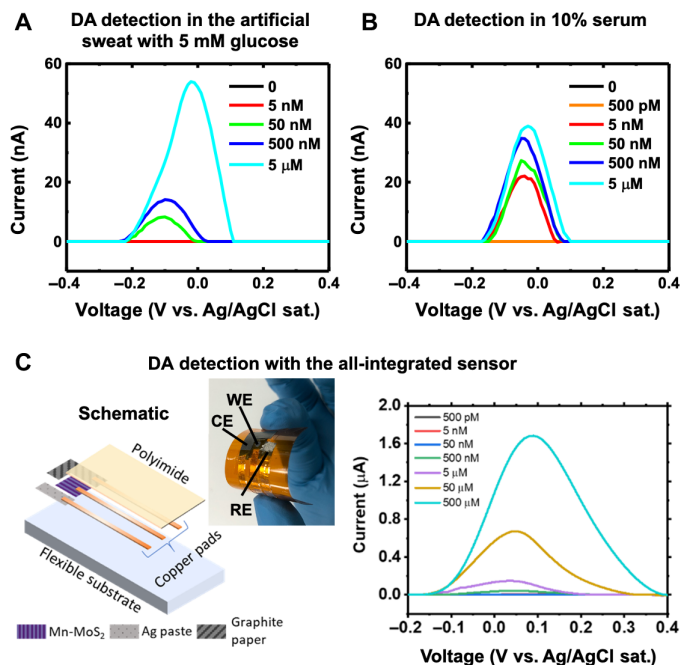


**Fig. 3. Detection of DA in biologically complex samples: artificial sweat and 10% serum and a proof-of-concept integrated sensor.** DPV results with DA in biologically complex samples: (A) artificial sweat containing 5 mM glucose and (B) 10% serum in PBS using Pt CE and Ag/AgCl RE. The Mn-MoS<sub>2</sub>/PGS sensor is able to detect 50 nM DA in artificial sweat with 5 mM glucose and 5 nM DA in 10% serum. (C) DA detection with an all-integrated sensor: a schematic of the all-integrated sensor fabricated on a polyimide (PI) sheet with on-chip WE, CE, and RE (inset: photograph of the fabricated sensor. Photo credit: D. Butler, Pennsylvania State University.) and the corresponding DPV results. The integrated sensor enables the detection of 500 nM DA in PBS.

defects considered are Mn substituting a sulfur atom ( $\text{Mn}_{\text{S}}$ ), Mn on top of a Mo atom ( $\text{Mn}_{\text{topMo}}$ ), two Mn atoms in the Mo site (denoted as Mn-split interstitial,  $2\text{Mn}_{\text{Si}}$ ), and Mn substituting a Mo atom ( $\text{Mn}_{\text{Mo}}$ ). Figure 4A plots the defect formation energy, revealing that  $\text{Mn}_{\text{topMo}}$ ,  $\text{Mn}_{\text{Si}}$ , and  $\text{Mn}_{\text{Mo}}$  are energetically possible. However, the formation energy of  $\text{Mn}_{\text{Mo}}$  is significantly lower than that of  $\text{Mn}_{\text{topMo}}$  and  $2\text{Mn}_{\text{Si}}$ , hence suggesting it to be the most abundant defect, which is consistent with the HAADF-STEM analysis (fig. S2). Although  $2\text{Mn}_{\text{Si}}$  is more favorable than  $\text{Mn}_{\text{topMo}}$ , the interaction with the DA molecule is less stable than if there were no defects; therefore,  $2\text{Mn}_{\text{Si}}$  is discarded. In other words, the molecule will not get anchored at this defect site.

To study the material interaction with DA, we consider both the  $\text{Mn}_{\text{topMo}}$  and substitutional  $\text{Mn}_{\text{Mo}}$  defects (schematically shown in Fig. 4B). The binding energy of DA to  $\text{Mn}_{\text{topMo}}$  is 2.91 eV, while the binding energy to the  $\text{Mn}_{\text{Mo}}$  is 0.65 eV, which is 0.02 eV larger than the binding to the defect-free MoS<sub>2</sub>. The exposed Mn in  $\text{Mn}_{\text{topMo}}$  allows it to strongly bind to the DA molecule because of the formation of Mn-C bonds with the aromatic ring of the DA. The large change in the density of states (DOS) after interaction with DA (fig. S9) confirms such strong interaction. The state belonging to the DA is at the valence band maximum of MoS<sub>2</sub>, with several states belonging to the  $\text{Mn}_{\text{topMo}}$  defect at higher energy (fig. S9). Holes from the MoS<sub>2</sub> would preferentially fill these defect states instead of oxidizing the DA molecules. This, coupled with the large binding energy, makes it unlikely that the DA molecule can be oxidized and then

**Table 1. A comparison of this work with recently reported electrochemical DA sensors.** Amp., chronoamperometry; CB, carbon black; CV, cyclic voltammetry; DPV, differential pulse voltammetry; HMS, hollow microspheres; ITO, indium tin oxide; LoD, limit of detection; LSG, laser-scribed graphene; NPs, nanoparticles; PABSA, poly(*m*-aminobenzenesulfonic acid); PBS, phosphate-buffered saline; PEDOT, poly(3,4-ethylenedioxythiophene); PET, polyethylene terephthalate; rGO, reduced graphene oxide; Ty, tyrosinase.

Material	Method	Medium	Sensing performance		References
			LoD ( $\mu\text{M}$ )	Dynamic range ( $\mu\text{M}$ )	
Cu <sub>2</sub> O HMS/CB	Amp.	PBS (pH 5.7)	$3.96 \times 10^{-2}$	$9.9 \times 10^{-2}$ to $7.08 \times 10^2$	(45)
WO <sub>3</sub> NPs/GCE	DPV	PBS (pH 7)	$2.4 \times 10^{-2}$	$10^{-1}$ to $5 \times 10^1$ , $5 \times 10^1$ to $6 \times 10^2$	(46)
PET/ITO/NiO NPs/Ty	CV	PBS (pH 6.5)	1.04	2 to $1 \times 10^2$	(47)
Graphene/diamond	DPV	PBS (0.1 M)	$2 \times 10^{-1}$	$5 \times 10^2$ to $2 \times 10^3$	(48)
LSG/PEDOT	DPV	PBS (pH 7.4)	$3.3 \times 10^{-1}$	$1 \times 10^2$ to $1.5 \times 10^2$	(49)
AuNPs@MoS <sub>2</sub>	DPV	PBS (pH 7)	$5 \times 10^{-2}$	$5 \times 10^{-2}$ to $3 \times 10^1$	(14)
PABSA-rMoS <sub>2</sub>	DPV	PBS (pH 7)	$2.2 \times 10^{-1}$	$1 \times 10^1$ to $5 \times 10^1$	(50)
MoS <sub>2</sub> /rGO/AuNPs	DPV	PBS (pH 7)	$1.1 \times 10^{-1}$	$3 \times 10^{-1}$ to $1.983 \times 10^2$	(51)
Mn-MoS <sub>2</sub> /PGS	DPV	PBS (pH 7.2)	$5 \times 10^{-5}$	$5 \times 10^{-5}$ to $5 \times 10^1$	This work
Mn-MoS <sub>2</sub> /PGS	DPV	Artificial sweat	$5 \times 10^{-2}$	$5 \times 10^{-2}$ to $5 \times 10^2$	
Mn-MoS <sub>2</sub> /PGS	DPV	10% serum	$5 \times 10^{-3}$	$5 \times 10^{-3}$ to $5 \times 10^2$	

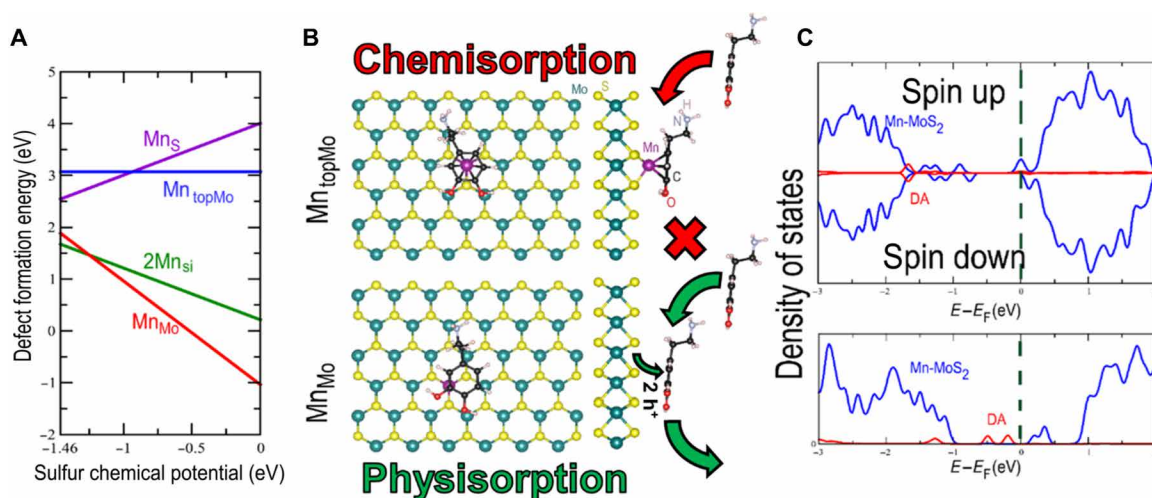


**Fig. 4. Density functional calculations.** (A) Formation energy of the Mn defects per Mn atom is shown for various defect configurations considered in this work. The substitutional defect Mn<sub>Mo</sub> is the lowest energy defect for most of the allowed chemical potential region. The least stable is the Mn<sub>S</sub> defect in which Mn atoms are substitutionally doped at the S sites. Mn<sub>Si</sub> represents the defects of two Mn atoms in the Mo site. (B) Top and side views of DA interacting with Mn<sub>topMo</sub> (neutral defect) forming a chemical bond and DA adsorbed (physisorbed) on Mn<sub>Mo</sub><sup>+</sup>. (C) Density of states (DOS) projected onto the DA molecule (in red) and the MoS<sub>2</sub> defective layer (in blue): The Mn<sub>topMo</sub> defect introduces impurity states in the bandgap, and the electrons close to the conduction band minimum will be available to generate a current in the device. Because Mn<sub>Mo</sub><sup>+</sup> is nonmagnetic, the spin up/down components are not shown separately. Here, states from the DA molecule sit in the middle of the gap slightly below the unoccupied Mn<sub>Mo</sub> defect states; thus, holes from MoS<sub>2</sub> can be preferentially transferred to these states, oxidizing the DA molecule.

released from the defect for efficient sensing. The Mn<sub>topMo</sub> defect generates a magnetic moment of  $3\mu_B$  in a supercell of 108 atoms; this magnetic state is 0.96 eV (per 108 supercells) more stable in energy than the nonmagnetic case.

The Mn<sub>Mo</sub> defect, on the other hand, only reacts with DA through physisorption with a carbon atom from the DA sitting above the Mn atom. Physisorption is critical in catalysis, as a catalytic material should ideally both adsorb the target species and efficiently desorb reaction by-products to allow for further catalytic reactions to take place (29). The DOS of the DA interacting with the

Mn<sub>Mo</sub><sup>+</sup> (Mn<sub>Mo</sub> defects in which Mn is +1 charge state) is shown in Fig. 4C. The neutral defect has one occupied level above DA. With the defect level in the +1 charge state, the occupied states with the highest energy now belong to the DA molecule. This ensures that holes will preferentially transfer to the DA molecule from the MoS<sub>2</sub>. Ionizing the defect allows the DA molecule to be oxidized, because the frontier orbitals now belong to the DA molecule, meaning that any hole from the MoS<sub>2</sub> will be transferred to the DA. The physisorption also ensures that the molecule can be removed after oxidation to allow other DA molecules to access the site.



## DISCUSSION

Elemental doping of TMDs for electrochemical biosensing applications remains relatively unexplored despite substantial efforts in other areas, such as electronics, thermoelectrics, and energy harvesting (e.g., hydrogen generation) (30–32). This is likely due to the seemingly endless combination of TMD parent compounds, dopants, and analytes, which presents researchers with the challenge of deciding which combinations are worthwhile. Furthermore, the introduction of dopants into the TMD lattice does not always have beneficial implications for catalysis and electrochemistry (32). Therefore, combined experimental and computational approaches, such as the work presented here, provide guidance in understanding how modulation of the electronic band structure can enhance the sensing behavior and realize such behavior experimentally.

In this work, we designed and fabricated highly sensitive electrochemical sensors for detection of DA using electrodeposited MoS<sub>2</sub> layers doped with Mn atoms. Using high-resolution TEM–STEM microscopy, we observe that the doping process results in different defect configurations: Mn atom on top of Mo (Mn<sub>topMo</sub>) and Mn substituting a Mo atom (Mn<sub>Mo</sub>), which are twice as abundant as the former. The enhanced sensing performance in the low concentration range (0 to 5 nM) is attributed to the affinity of Mn<sub>Mo</sub> to physically adsorb DA, while the contribution of Mn<sub>topMo</sub> defects increases at higher concentrations (5 nM to 5 mM). While Mn<sub>topMo</sub> defects form a chemical bond with DA (i.e., chemisorbed), the probability of hole transfer to DA is miniscule, meaning that oxidation will not occur. However, for the Mn<sub>Mo</sub> defect, which is more stable than the Mn<sub>topMo</sub> defect, the DA is physisorbed and the probability of hole transfer to the DA is higher. Hence, this defect configuration is able to oxidize DA more readily. Future investigations into other elemental dopants (e.g., Cu, Fe, Co, and Ni) and their effect on charge transfer and biosensor response are certainly warranted. As a result of the improved electronic characteristics from doping, the electrochemical sensors based on Mn-doped MoS<sub>2</sub> are capable of DA detection down to 50 pM in PBS at neutral pH, which is four orders of magnitude lower than that of undoped MoS<sub>2</sub>. Electrochemical analysis using various redox probes confirms that the addition of Mn improves the charge transfer kinetics compared to bare PGS and undoped MoS<sub>2</sub>. The sensor is also selective toward DA when compared to AA and UA and is able to detect as little as 50 nM DA in sweat and 5 nM in serum.

While the sensor response to UA is much less than for DA, the overlapping peaks could present some minor complications and addressing this issue could be the subject of a future study. Aside from doping (as discussed here), other strategies for enhancing selectivity to DA include surface functionalization [e.g., enzymes (tyrosinase) (33), aptamers (34), and metal/metal oxide nanoparticles (35)], incorporation of ionic liquids into the sensor (36), and advanced voltammetric techniques [such as fast-scan CV (37)]. These techniques each come with their respective pros and cons. For example, enzymatic sensors display a high degree of selectivity but can suffer from long-term environmental instabilities and require immobilization of the enzyme on the sensor surface, which introduces a new set of fabrication challenges (38) and may limit scalability. Although no method poses as a perfect solution, the present work opens up avenues for the engineering of 2D and layered systems in bioelectronics with enhanced sensing performance through tuning of the material properties, thereby allowing for more sensitive and selective analyte detection. Despite electrochemical sensors being the

first successfully commercialized biosensor technology—specifically glucose sensors—to the best of our knowledge, there are no commercially available electrochemical DA sensors available. Hence, we believe that the contributions presented here help serve the materials and biosensor communities, as well as the broader research community, in transitioning toward novel point-of-care applications.

## MATERIALS AND METHODS

### Material synthesis

MoS<sub>2</sub> electrodeposition was performed using ammonium tetrathiomolybdate [99.97%, 1 mg ml<sup>−1</sup>; (NH<sub>4</sub>)<sub>2</sub>MoS<sub>4</sub>; Sigma-Aldrich] and potassium chloride (>99%, 1 mg ml<sup>−1</sup>; KCl; Sigma-Aldrich, supporting electrolyte) aqueous solution as the electrolyte. Pt wire was used as the CE, Ag/AgCl (sat. KCl) as the RE, and the PGS as the WE. To reduce the MoS<sub>4</sub><sup>2−</sup> anions into amorphous MoS<sub>2</sub>, a potentiostatic deposition was performed for 1 hour at −0.8 V (versus Ag/AgCl). Subsequently, the deposited MoS<sub>2</sub>/PGS was placed into a small quartz tube, next to the Mn precursor (60 mg of manganese acetate). The small quartz tube with MoS<sub>2</sub>/PGS and the Mn precursor were then transferred to the middle of a larger quartz tube with a diameter of 1 cm for doping/annealing. To avoid the oxidation of MoS<sub>2</sub> during the doping/annealing, sulfur powder (1 g) was heated separately using a heating belt at the upstream of the tube, and the system was purged with Ar [300 standard cubic centimeter per minute (sccm)] for 15 min. The temperature ramp for the sulfur powder was as follows: heat up to 70°C in 10 min with a 30-min dwell time, then further heating to 250°C in 6 min, and dwell time for 20 min followed by cooling down naturally to room temperature. The tube furnace was first ramped to 500°C in 20 min and then heated to 800°C for another 20 min, followed by a 30-min dwell time. The Ar flow was 100 sccm during the synthesis. Last, the furnace was cooled down to room temperature naturally. Pristine MoS<sub>2</sub> samples were prepared using the same conditions without using the Mn precursor.

### Material characterization

Mn-doped MoS<sub>2</sub> film on graphite paper (Mn–MoS<sub>2</sub>/PGS) was transferred to a Quantifoil TEM grid by scratching the surface of Mn–MoS<sub>2</sub>/PGS. The scratched flakes were dispersed into ethanol and sonicated for 10 s, and then the solution was dropped onto a Quantifoil TEM grid. TEM was carried out using a FEI Titan<sup>3</sup> G2 S/TEM operating at 80 kV. A HAADF detector was used for STEM-ADF imaging. For most images in this work, a Gaussian blur filter ( $r = 2.00$ ) was applied by the ImageJ program to reduce noise and enhance the visibility of the structural details. STEM-ADF image simulation was conducted by the QSTEM package (39). Simulation parameters, such as acceleration voltage, spherical aberration (C<sub>3</sub> and C<sub>5</sub>), and convergence angle and inner/outer angle for the HAADF detector, were set according to the experimental conditions.

XPS measurements were conducted in a high-resolution Thermo Scientific XPS with a monochromatic Al K $\alpha$  x-ray source. The resulting spectra were charge-referenced to adventitious carbon corresponding to the carbon 1s peak at 284.8 eV. Raman spectroscopy measurements were performed using an inVia confocal Renishaw Raman spectrometer. A 100 $\times$  objective lens and a 488-nm wavelength laser were used to excite the samples. The spectrometer was calibrated using a standard Si sample before the measurements. XRD was

performed using a PANalytical Empyrean x-ray diffractometer with a scanning range from 5° to 80°.

### Electrochemical characterization

Electrochemical tests, including EIS, CV, and DPV, were recorded using a PalmSens4 potentiostat, in conjunction with PSTrace5 software (BASi Co., USA), and a three-electrode system. A Pt wire and Ag/AgCl (sat. NaCl) were used as the CE and RE, respectively (unless otherwise stated). Test devices were prepared by contacting the sensing material with the copper tape. A small exposed window (~2 mm<sup>2</sup>) was isolated using the PI tape. CV and EIS are used for characterizing electron transfer kinetics and the reversibility of reactions (23). [Fe(CN)<sub>6</sub>]<sup>3-/4-</sup> and [Ru(NH<sub>3</sub>)<sub>6</sub>]<sup>2+/3+</sup> [both 5 mM in PBS (pH 7)] were used as redox probes for the CV measurements. The solution (100 µl) was pipetted onto the electrode, and the potential was scanned from -0.6 to 0.6 versus Ag/AgCl at a scan rate of 50 mV/s. For EIS measurements, a 50 µM DA solution [in PBS (pH 7)] was used as the redox probe to specifically investigate the charge transfer characteristics relating to the redox of DA. A DC potential of 0.1 V versus OCP was applied in addition to an AC potential of 10 mV. The frequency was swept over a range of 1 MHz to 1 mHz. OCP is determined by the potentiostat before the measurement is started. A Newton algorithm was used to fit the equivalent circuit and obtain the charge transfer resistance.

For quantitative identification, DA or the interfering metabolites (UA and AA) were dissolved at a given concentration in the electrolyte [PBS (pH 7) or artificial sweat]. The DPV was performed from -0.6 to 0.4 V with a potential step of 10 mV, a pulse potential of 200 mV, a pulse time of 20 ms, and a scan rate of 50 mV/s. The peak values of the DPV spectra were read after a polynomial spline baseline correction (40). The baseline was defined as the signal obtained for the analyte-free electrolyte solution. We defined the signal as the normalized peak current, written as  $I_n \triangleq \frac{I}{I_{\max}} \times 100\%$ ,

where  $I$  is defined as the peak current for a given sample at a given DA concentration ( $\rho_{\text{DA}}$ ) and  $I_{\max}$  is defined as the peak current for the same sample at a DA concentration of 50 µM in PBS. To obtain error bars, each concentration was measured using three distinct sensors synthesized under the same material synthesis condition. Amperometric measurements were carried out in a three-electrode electrochemical cell with 15 ml of solution. The sensor current was allowed to stabilize before any analytes were added. The solution was held under constant stirring at 450 rpm. Analytes were added every 50 s without pausing of the amperometric scan.

The artificial sweat solution was prepared similarly to the report by Gao *et al.* (41). The solution was made up of 22 mM urea, 5.5 mM lactic acid, 3 mM NH<sub>4</sub><sup>+</sup>, 0.4 mM Ca<sup>2+</sup>, 50 µM Mg<sup>2+</sup>, 25 µM UA, 5 mM glucose, 10 mM K<sup>+</sup>, and 100 mM Na<sup>+</sup>. All chemicals were purchased from Sigma-Aldrich, USA. The pH of the solution was adjusted to slightly under 7, which falls within the typical range of pH 5 to 7. The serum solution was prepared using fetal bovine serum (Corning, USA; U.S. origin, no heat inactivation) diluted 1:10 in PBS.

The all-integrated sensor was fabricated on a flexible PI substrate. Mn-MoS<sub>2</sub> was used as the WE. A 2-mm-diameter biopsy punch was used to create a window in the PI tape before placing onto the WE, thus allowing for consistent geometric area across sensors. Adhesive PGS were used as the basis of the RE and CE. The RE was formed by depositing colloidal Ag paste (Electron Microscopy Sciences, USA)

onto the graphite sheet to serve as the pseudo-RE. The paste was cured at 120°C in an oven for 30 min, as per the manufacturer's recommendation, before measurements were taken. Here, the copper tape was used to electrically contact each electrode. The PI tape was used to electrically isolate the electrodes from the copper tape. For electrochemical measurements, ~300 µl of solution was used to ensure that all electrodes were completely immersed.

### DFT calculations

DFT calculations were done using Quantum Espresso (42) with the local density approximation (LDA) (43) and the projector-augmented wave (PAW) (44) method. A plane wave basis up to an energy cutoff of 544 eV was used for the wave functions. A 6 × 6 supercell of monolayer MoS<sub>2</sub> was used with a 3 × 3 gamma-centered k-point grid. The cell was 22 Å long in the perpendicular direction, and spin polarization was considered for all calculations. The convergence criterion for the self-consistent calculations was 10<sup>-6</sup> eV, and the atomic positions were relaxed until all the forces were under 0.01 eV/Å. Formation energies are calculated as Eq. 4

$$E_F = (E_{\text{Defect}} + \mu_A) - (E_{\text{Pristine}} + \mu_{\text{Mn}}) \quad (4)$$

where  $\mu_{\text{Mn}}$  is the energy of a Mn atom in the bulk phase and  $\mu_A$  is the chemical potential of the S or Mo atom that is removed from the cell.  $E_{\text{Defect}}$  and  $E_{\text{Pristine}}$  are the total energies of the defective and nondefective MoS<sub>2</sub> supercells, respectively.

### SUPPLEMENTARY MATERIALS

Supplementary material for this article is available at <http://advances.sciencemag.org/cgi/content/full/6/32/eabc4250/DC1>

### REFERENCES AND NOTES

1. D. F. Sharman, The catabolism of catecholamines: Recent studies. *Br. Med. Bull.* **29**, 110–115 (1973).
2. M. A. Piggott, E. F. Marshall, N. Thomas, S. Lloyd, J. A. Court, E. Jaros, D. Burn, M. Johnson, R. H. Perry, I. G. McKeith, C. Ballard, E. K. Perry, Striatal dopaminergic markers in dementia with Lewy bodies, Alzheimer's and Parkinson's diseases: Rostrocaudal distribution. *Brain* **122**, 1449–1468 (1999).
3. E. D. Bird, E. G. Spokes, L. L. Iversen, Increased dopamine concentration in limbic areas of brain from patients dying with schizophrenia. *Brain* **102**, 347–360 (1979).
4. A. El-Beqqali, A. Kussak, M. Abdel-Rehim, Determination of dopamine and serotonin in human urine samples utilizing microextraction online with liquid chromatography/electrospray tandem mass spectrometry. *J. Sep. Sci.* **30**, 421–424 (2007).
5. S. Su, H. F. Sun, F. Xu, L. H. Yuwen, L. H. Wang, Highly sensitive and selective determination of dopamine in the presence of ascorbic acid using gold nanoparticles-decorated MoS<sub>2</sub> nanosheets modified electrode. *Electroanalysis* **25**, 2523–2529 (2013).
6. J. W. M. Lenders, K. Pacak, M. M. Walther, W. M. Linehan, M. Mannelli, P. Friberg, H. R. Keiser, D. S. Goldstein, G. Eisenhofer, Biochemical diagnosis of pheochromocytoma: Which test is best? *JAMA* **287**, 1427–1434 (2002).
7. T. Qian, C. Yu, X. Zhou, S. Wu, J. Shen, Au nanoparticles decorated polypyrrole/reduced graphene oxide hybrid sheets for ultrasensitive dopamine detection. *Sens. Actuators B* **193**, 759–763 (2014).
8. C. Z. Zhu, D. Dan, Y. H. Lin, Graphene and graphene-like 2D materials for optical biosensing and bioimaging: A review. *2D Mater.* **2**, 032004 (2015).
9. R. Kurapati, K. Kostarelos, M. Prato, A. Bianco, Biomedical uses for 2D materials beyond graphene: Current advances and challenges ahead. *Adv. Mater.* **28**, 6052–6074 (2016).
10. J. Ortiz-Medina, F. López-Urías, H. Terrones, F. J. Rodríguez-Macías, M. Endo, M. Terrones, Differential response of doped/defective graphene and dopamine to electric fields: A density functional theory study. *J. Phys. Chem. C* **119**, 13972–13978 (2015).
11. K. S. Novoselov, A. K. Geim, S. V. Morozov, D. Jiang, Y. Zhang, S. V. Dubonos, I. V. Grigorieva, A. A. Firsov, Electric field effect in atomically thin carbon films. *Science* **306**, 666–669 (2004).



12. K. Kalantar-zadeh, J. Z. Ou, T. Daeneke, M. S. Strano, M. Pumera, S. L. Gras, Two-dimensional transition metal dichalcogenides in biosystems. *Adv. Funct. Mater.* **25**, 5086–5099 (2015).
13. K. F. Mak, C. Lee, J. Hone, J. Shan, T. F. Heinz, Atomically thin MoS<sub>2</sub>: A new direct-gap semiconductor. *Phys. Rev. Lett.* **105**, 4 (2010).
14. H. Sun, J. Chao, X. Zuo, S. Su, X. Liu, L. Yuwen, C. Fan, L. Wang, Gold nanoparticle-decorated MoS<sub>2</sub> nanosheets for simultaneous detection of ascorbic acid, dopamine and uric acid. *RSC Adv.* **4**, 27625–27629 (2014).
15. C. Ataca, S. Ciraci, Functionalization of single-layer MoS<sub>2</sub> honeycomb structures. *J. Phys. Chem. C* **115**, 13303–13311 (2011).
16. R. V. Lloyd, Mechanism of the manganese-catalyzed autoxidation of dopamine. *Chem. Res. Toxicol.* **8**, 111–116 (1995).
17. T. M. Florence, J. L. Stauber, Manganese catalysis of dopamine oxidation. *Sci. Total Environ.* **78**, 233–240 (1989).
18. J. Suh, T.-E. Park, D.-Y. Lin, D. Fu, J. Park, H. J. Jung, Y. Chen, C. Ko, C. Jang, Y. Sun, R. Sinclair, J. Chang, S. Tongay, J. Wu, Doping against the native propensity of MoS<sub>2</sub>: Degenerate hole doping by cation substitution. *Nano Lett.* **14**, 6976–6982 (2014).
19. D. B. Williams, C. B. Carter, in *Transmission Electron Microscopy* (Springer, 1996), pp. 3–17.
20. T. X. Wang, W. W. Chen, Low-temperature synthesis of pure rock-salt structure manganese sulfide using a single-source molecular precursor. *Chem. Eng. J.* **144**, 146–148 (2008).
21. K. H. Zhang, S. Feng, J. Wang, A. Azcatl, N. Lu, R. Addou, N. Wang, C. Zhou, J. Lerach, V. Bojan, M. J. Kim, L.-Q. Chen, R. M. Wallace, M. Terrones, J. Zhu, J. A. Robinson, Manganese doping of monolayer MoS<sub>2</sub>: The substrate is critical. *Nano Lett.* **15**, 6586–6591 (2015).
22. R. L. McCreery, Advanced carbon electrode materials for molecular electrochemistry. *Chem. Rev.* **108**, 2646–2687 (2008).
23. A. J. Bard, L. R. Faulkner, J. Leddy, C. G. Zoski, *Electrochemical Methods: Fundamentals and Applications* (Wiley, 1980), vol. 2.
24. P. R. Roy, T. Okajima, T. Ohsaka, Simultaneous electroanalysis of dopamine and ascorbic acid using poly (*N,N*-dimethylaniline)-modified electrodes. *Bioelectrochemistry* **59**, 11–19 (2003).
25. B.-Y. Chang, S.-M. Park, Electrochemical impedance spectroscopy. *Annu. Rev. Anal. Chem.* **3**, 207–229 (2010).
26. T. Kiliç, A. T. D. S. Valinhas, I. Wall, P. Renaud, S. Carrara, Label-free detection of hypoxia-induced extracellular vesicle secretion from MCF-7 cells. *Sci. Rep.* **8**, 9402 (2018).
27. A. N. Patel, S.-y. Tan, T. S. Miller, J. V. Macpherson, P. R. Unwin, Comparison and reappraisal of carbon electrodes for the voltammetric detection of dopamine. *Anal. Chem.* **85**, 11755–11764 (2013).
28. S. Robinson, A. H. Robinson, Chemical composition of sweat. *Physiol. Rev.* **34**, 202–220 (1954).
29. J. D. Benck, T. R. Hellstern, J. Kibsgaard, P. Chakthranont, T. F. Jaramillo, Catalyzing the hydrogen evolution reaction (HER) with molybdenum sulfide nanomaterials. *ACS Catal.* **4**, 3957–3971 (2014).
30. N. Rohaizad, C. C. Mayorga-Martinez, Z. Sofer, R. D. Webster, M. Pumera, Niobium-doped TiS<sub>2</sub>: Formation of TiS<sub>3</sub> nanobelts and their effects in enzymatic biosensors. *Biosens. Bioelectron.* **155**, 112114 (2020).
31. A. A. Tedstone, D. J. Lewis, P. O'Brien, Synthesis, properties, and applications of transition metal-doped layered transition metal dichalcogenides. *Chem. Mater.* **28**, 1965–1974 (2016).
32. S. M. Tan, M. Pumera, Two-dimensional materials on the rocks: Positive and negative role of dopants and impurities in electrochemistry. *ACS Nano* **13**, 2681–2728 (2019).
33. J. Njagi, M. M. Chernov, J. C. Leiter, S. Andreescu, Amperometric detection of dopamine in vivo with an enzyme based carbon fiber microbiosensor. *Anal. Chem.* **82**, 989–996 (2010).
34. S. Liu, X. Xing, J. Yu, W. Lian, J. Li, M. Cui, J. Huang, A novel label-free electrochemical aptasensor based on graphene–polyaniline composite film for dopamine determination. *Biosens. Bioelectron.* **36**, 186–191 (2012).
35. B. J. Plowman, M. Mahajan, A. P. O'Mullane, S. K. Bhargava, Electrochemical detection of dopamine and cytochrome c at a nanostructured gold electrode. *Electrochim. Acta* **55**, 8953–8959 (2010).
36. Y. Li, X. Liu, W. Wei, Square wave voltammetry for selective detection of dopamine using polyglycine modified carbon ionic liquid electrode. *Electroanalysis* **23**, 2832–2838 (2011).
37. P. E. M. Phillips, R. M. Wightman, Critical guidelines for validation of the selectivity of *in-vivo* chemical microsenors. *TRAC Trends Anal. Chem.* **22**, 509–514 (2003).
38. K. Jackowska, P. Kryszynski, New trends in the electrochemical sensing of dopamine. *Anal. Bioanal. Chem.* **405**, 3753–3771 (2013).
39. C. T. Koch, "Determination of core structure periodicity and point defect density along dislocations," thesis, Arizona State University, 2002.
40. M. Jakubowska, Signal processing in electrochemistry. *Electroanalysis* **23**, 553–572 (2011).
41. W. Gao, S. Emaminejad, H. Y. Y. Nyein, S. Challa, K. Chen, A. Peck, H. M. Fahad, H. Ota, H. Shiraki, D. Kiriya, D.-H. Lien, G. A. Brooks, R. W. Davis, A. Javey, Fully integrated wearable sensor arrays for multiplexed *in situ* perspiration analysis. *Nature* **529**, 509 (2016).
42. P. Giannozzi, O. Andreussi, T. Brumme, O. Bunau, M. B. Nardelli, M. Calandra, R. Car, C. Cavazzoni, D. Ceresoli, M. Cococcioni, N. Colonna, I. Carnimeo, A. D. Corso, S. de Gironcoli, P. Delugas, R. A. Di Stasio, A. Ferretti, A. Floris, G. Fratesi, G. Fugallo, R. Gebauer, U. Gerstmann, F. Giustino, T. Gorni, J. Jia, M. Kawamura, H.-Y. Ko, A. Kokalj, E. Küçükbenli, M. Lazzeri, M. Marsili, N. Marzari, F. Mauri, N. L. Nguyen, H.-V. Nguyen, A. Otero-de-la-Roza, L. Paulatto, S. Poncè, D. Rocca, R. Sabatini, B. Santra, M. Schlipf, A. P. Seitsonen, A. Smogunov, I. Timrov, T. Thonhauser, P. Umari, N. Vast, X. Wu, S. Baroni, Advanced capabilities for materials modelling with Quantum ESPRESSO. *J. Phys. Condens. Matter* **29**, 465901 (2017).
43. J. P. Perdew, Y. Wang, Accurate and simple analytic representation of the electron-gas correlation energy. *Phys. Rev. B* **45**, 13244 (1992).
44. P. E. Blöchl, Projector augmented-wave method. *Phys. Rev. B* **50**, 17953 (1994).
45. L.-N. Wu, Y.-L. Tan, L. Wang, S.-N. Sun, Z.-Y. Qu, J.-M. Zhang, Y.-J. Fan, Dopamine sensor based on a hybrid material composed of cuprous oxide hollow microspheres and carbon black. *Microchim. Acta* **182**, 1361–1369 (2015).
46. A. C. Anithaa, N. Lavanya, K. Asokan, C. Sekar, WO<sub>3</sub> nanoparticles based direct electrochemical dopamine sensor in the presence of ascorbic acid. *Electrochim. Acta* **167**, 294–302 (2015).
47. A. Roychoudhury, S. Basu, S. K. Jha, Dopamine biosensor based on surface functionalized nanostructured nickel oxide platform. *Biosens. Bioelectron.* **84**, 72–81 (2016).
48. Q. Yuan, Y. Liu, C. Ye, H. Sun, D. Dai, Q. Wei, G. Lai, T. Wu, A. Yu, L. Fu, K. W. A. Chee, C.-T. Lin, Highly stable and regenerative graphene-diamond hybrid electrochemical biosensor for fouling target dopamine detection. *Biosens. Bioelectron.* **111**, 117–123 (2018).
49. G. Y. Xu, Z. A. Jarjesa, V. Desprez, P. A. Kilmartin, J. Travas-Sejdic, Sensitive, selective, disposable electrochemical dopamine sensor, based on PEDOT-modified laser scribed graphene. *Biosens. Bioelectron.* **107**, 184–191 (2018).
50. T. Yang, H. Chen, C. Jing, S. Luo, W. Li, K. Jiao, Using poly(*m*-aminobenzenesulfonic acid)-reduced MoS<sub>2</sub> nanocomposite synergistic electrocatalysis for determination of dopamine. *Sens. Actuat. B Chem.* **249**, 451–457 (2017).
51. Y. A. Zhao, J. Zhou, Z. Jia, D. Huo, Q. Liu, D. Zhong, Y. Hu, M. Yang, M. Bian, C. Hou, In-situ growth of gold nanoparticles on a 3D-network consisting of a MoS<sub>2</sub>/rGO nanocomposite for simultaneous voltammetric determination of ascorbic acid, dopamine and uric acid. *Microchim. Acta* **186**, 92 (2019).

#### Acknowledgments

**Funding:** We would like to thank the Materials Research Institute at the Pennsylvania State University and their staff for their assistance with the material characterization. We also acknowledge S. Subramanian for help in the first XPS measurement. Y.L., D.B., M.T., and A.E. would like to acknowledge the NSF/UCRC ATOMIC program for support (award #1540018). A.E. also acknowledges the Start-up Fund from the Pennsylvania State University. M.C.L. and H.T. are grateful to the NSF (EFRI-1433311). The supercomputer time was provided by the Center for Computational Innovations (CCI) at Rensselaer Polytechnic Institute and the Extreme Science and Engineering Discovery Environment (XSEDE; project TG-DMR17008), which is supported by NSF grant number ACI-1053575. **Author contributions:** Y.L. and D.B. wrote the manuscript and performed the electrochemical experiments. Y.L. synthesized the materials. F.Z. and K.F. assisted with the TEM/STEM studies. T.X. assisted with the electrochemical measurements. T.G.-N., R.C.-S., and M.E. helped with the XPS measurements. M.C.L. and H.T. performed the DFT calculations, contributed to the manuscript, and provided theoretical insight. A.E. and M.T. designed and supervised the research. **Competing interests:** The authors declare that they have no competing interests. **Data and materials availability:** All data needed to evaluate the conclusions in the paper are present in the paper and/or the Supplementary Materials. Additional data related to this paper may be requested from the authors.

Submitted 23 April 2020

Accepted 25 June 2020

Published 7 August 2020

10.1126/sciadv.abc4250

**Citation:** Y. Lei, D. Butler, M. C. Lucking, F. Zhang, T. Xia, K. Fujisawa, T. Granzier-Nakajima, R. Cruz-Silva, M. Endo, H. Terrones, M. Terrones, A. Ebrahimi, Single-atom doping of MoS<sub>2</sub> with manganese enables ultrasensitive detection of dopamine: Experimental and computational approach. *Sci. Adv.* **6**, eabc4250 (2020).